



Article

Cu₂Se Nanoparticles Encapsulated by Nitrogen-Doped Carbon Nanofibers for Efficient Sodium Storage

Le Hu ^{1,†} , Chaoqun Shang ^{1,*,†} , Eser Metin Akinoglu ² , Xin Wang ^{1,2,*} and Guofu Zhou ^{1,2}

¹ National Center for International Research on Green Optoelectronics, South China Normal University, Guangzhou 510006, China; hule@m.scnu.edu.cn (L.H.); guofu.zhou@m.scnu.edu.cn (G.Z.)

² International Academy of Optoelectronics at Zhaoqing, South China Normal University, Zhaoqing 526060, China; e.akinoglu@zq-scnu.org

* Correspondence: chaoqun.shang@ecs-scnu.org (C.S.); wangxin@scnu.edu.cn (X.W.)

† These authors contributed equally to this work.

Received: 13 January 2020; Accepted: 7 February 2020; Published: 10 February 2020



Abstract: Cu₂Se with high theoretical capacity and good electronic conductivity have attracted particular attention as anode materials for sodium ion batteries (SIBs). However, during electrochemical reactions, the large volume change of Cu₂Se results in poor rate performance and cycling stability. To solve this issue, nanosized-Cu₂Se is encapsulated in 1D nitrogen-doped carbon nanofibers (Cu₂Se-NC) so that the unique structure of 1D carbon fiber network ensures a high contact area between the electrolyte and Cu₂Se with a short Na⁺ diffusion path and provides a protective matrix to accommodate the volume variation. The kinetic analysis and D_{Na⁺} calculation indicates that the dominant contribution to the capacity is surface pseudocapacitance with fast Na⁺ migration, which guarantees the favorable rate performance of Cu₂Se-NC for SIBs.

Keywords: sodium ion batteries; Cu₂Se-NC; carbon nanofibers; rate capability; cycling stability

1. Introduction

Sodium-ion batteries (SIBs) have garnered tremendous attention due to the low price and abundance of sodium resources, and are considered as one of the promising alternatives to commercial lithium-ion batteries [1–3]. However, the large ionic radius of Na⁺ causes huge volume variation during Na⁺ insertion/extraction, which results in sluggish reaction kinetics and undesirable electrochemical performance [4,5]. Thus, the exploration of suitable electrode materials is still a great challenge for effective and reversible accommodation of large Na⁺ for wide-scale practical application of SIBs [6,7].

Among various potential electrode material candidates for SIBs, metal selenides have attracted particular attention because of good electronic conductivity and high reversible capacity based on multielectron conversion reactions [8,9]. Lou et al. prepared Cu-doped CoSe₂ microboxes with high reversible capacity of 492 mAh g⁻¹, excellent rate capability and long cycling life [10]. Yang and co-workers synthesized a 3D trilayer (CNT/MoSe₂/C) as freestanding electrodes with high areal capacity (4.0 mAh cm⁻²) and promising cycling stability [11]. Compared to MSe₂ with high Se content, M₂Se such as Cu₂Se with an inactive Cu component has the advantages of high electronic conductivity, structural stability and low volume variation during cycling [12–14]. However, most of these alternatives suffer from large volume changes during the conversion reaction with unsatisfied electrochemical performances [15,16]. As an effective approach, designing nanostructured materials can increase the active sites and specific surface area, further improving the reaction kinetics and reversible specific capacity [17]. Nevertheless, nanomaterials tend to agglomerate during cycling, which still prevents the long-term cycle life

of the batteries. To solve these issues, the common tactic is to synthesize metal selenide/carbon nanocomposites [18]. Nanosized active materials uniformly dispersed in carbon matrix can effectively inhibit aggregation of the nanoparticles and alleviate the volume expansion caused by Na^+ insertion [19–21].

In this paper, Cu_2Se nanoparticles are embedded in 1D nitrogen doped carbon nanofibers ($\text{Cu}_2\text{Se-NC}$). The unique structure of 1D carbon fiber can shorten the Na^+ diffusion path with a high contact area between Cu_2Se and the electrolyte. Meanwhile, carbon conductive network provides a buffering matrix for the effective accommodation of volume variation and alleviates the aggregation of Cu_2Se nanoparticles to maintain the structural integrity during repeated cycling. Based on these favorable effects, $\text{Cu}_2\text{Se-NC}$ displays a promising rate capability and long-term cycling life for efficient sodium storage.

2. Experimental Section

2.1. Preparation of $\text{Cu}_2\text{Se-NC}$ Nanofibers

A solution containing 10 mL dimethylformamide (DMF, Aladdin, Shanghai, China), 0.4 g $\text{Cu}(\text{CH}_3\text{COO})_2 \cdot \text{H}_2\text{O}$ (Aladdin), and 0.8 g polyacrylonitrile (PAN, $M_w = 150,000$, Aldrich, St. Louis, MO, USA) was vigorously stirred for about 12 h, which was then loaded into a 20-mL syringe with 19-G needle for electrospinning. The electrospinning process was applied voltage of 1 kV cm^{-1} with flow rate of $10 \mu\text{L min}^{-1}$. After electrospinning, the collected $\text{Cu}(\text{AC})_2/\text{PAN}$ nanofibers were selenized with Se powder (mass ratio of 1:2) in tube furnace at $500 \text{ }^\circ\text{C}$ for 4 h (Ar/H_2 atmosphere, heating rate: $2 \text{ }^\circ\text{C min}^{-1}$) to obtain $\text{Cu}_2\text{Se-NC}$. The Cu_2Se and nitrogen doped carbon nanofibers (NC) were acquired through the similar treatment procedure by using $\text{Cu}(\text{AC})_2$ with Se powder and PAN nanofibers, respectively.

2.2. Material Characterization

Field emission scanning electron microscope (FESEM, ZEISS Ultra 55, Carl Zeiss Inc., Oberkochen, Germany) and transmission electron microscope (TEM, JEM-2100F, JEOL Ltd., Tokyo, Japan) were used to observe morphology and structure. X-ray diffraction patterns (XRD, Bruker D8 Advance, Karlsruhe, Germany) and X-ray photoelectron spectroscopy (XPS, PHI 5600, Physical electronics, Chanhassen, MN, USA) were conducted to analyze the phase structure and chemical composition, respectively. Thermal gravimetric analysis (TGA, SDT Q600 TG-DTA, TA Instruments-Waters LLC, New Castle, DE, USA) was performed from room temperature to $600 \text{ }^\circ\text{C}$ (air, $10 \text{ }^\circ\text{C min}^{-1}$).

2.3. Electrochemical Measurements

The slurry composed of 80 wt% active material, 10 wt% Super P, 10 wt% polyvinylidene fluoride (PVDF) dispersed in appropriate *N*-methyl-2-pyrrolidone (NMP) was cast onto copper foil as electrode with active material loading of about $0.8\text{--}1.0 \text{ mg cm}^{-2}$. The electrolyte was 1 M NaClO_4 , which dissolved in a solution of ethylene carbonate (EC) and dimethyl carbonate (DMC) with volume ratio of 1:1 as well as additive of 5 wt% fluoroethylene carbonate (FEC). The electrochemical performances tests were measured by a Neware battery testing system in a voltage window of 0.1–3.0 V. Cyclic voltammetry (CV) and electrochemical impedance spectroscopy (EIS) conducted on an electrochemical workstation (BioLogic VMP3, Bio-Logic, Seyssinet-Pariset, France).

3. Results and Discussion

As shown in Figure 1a, the morphology of the as-electrospun $\text{Cu}(\text{AC})_2/\text{PAN}$ is composed of highly uniform and smooth nanofibers with diameter of $\sim 200 \text{ nm}$. The selenized nanofibers maintained the 1D structure, where Cu_2Se nanoparticles are uniformly distributed in the carbon nanofibers (Figure 1b,c). The appropriate void space between as-prepared $\text{Cu}_2\text{Se-NC}$ nanofibers is beneficial to the penetration of electrolyte. The low-resolution TEM images reveal that Cu_2Se nanoparticles were homogeneously

embedded in the carbon nanofibers in Figure 1d, and further confirm the structural feature of Cu₂Se-NC, agreeing well with the SEM results. A high-resolution TEM (HRTEM) image reveals the crystal phase of Cu₂Se possess good crystallinity, and the lattice spacing of 0.204 nm is ascribed to the (220) crystal plane of Cu₂Se (Figure 1e). Additionally, the selected area electron diffraction (SAED) of Cu₂Se-NC indicates the formation of Cu₂Se with polycrystallinity (Figure 1f). SEM image and corresponding EDX mapping results shown in Figure 1g,h reveal the uniform distribution of Cu, Se, N, and C throughout the nanofibers. However, bulk Cu₂Se is composed of irregular nanoparticles in the absence of carbon nanofiber support (Figure S1).

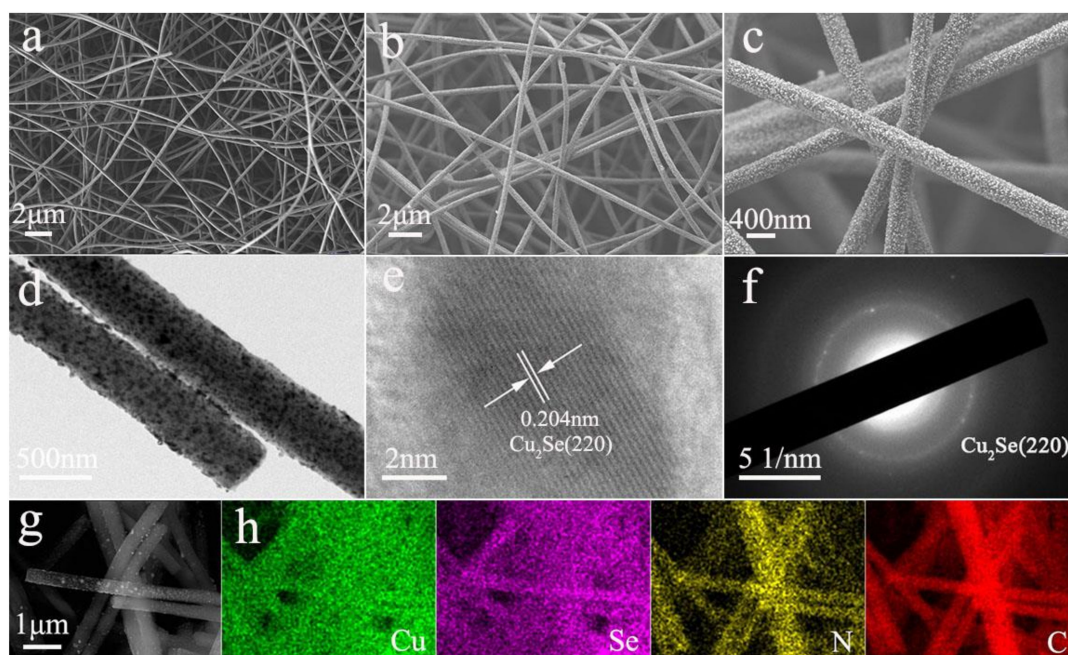


Figure 1. (a) SEM image of Cu(AC)₂/PAN electrospun nanofibers; (b,c) SEM and (d) TEM images of Cu₂Se-NC nanofibers after selenization treatment; (e) HRTEM image of Cu₂Se-NC nanofibers. (f) Selected-area electron diffraction patterns of Cu₂Se-NC nanofibers. (g) SEM image and (h) corresponding elemental mappings of Cu, Se, N, and C of Cu₂Se-NC.

The X-ray diffraction (XRD) pattern of as-prepared Cu₂Se-NC is displayed in Figure 2a. The major diffraction peaks at 26.8, 31.0, 44.5, 52.6, 64.7 and 81.9° are ascribed to (111), (200), (220), (311), (400) and (422) lattice planes of Cu₂Se (JCPDS No. 65-2982), which proves successful synthesis of Cu₂Se phase. In addition, a sharp and strong (220) peak indicates significantly crystallinity and in good agreement with the HRTEM and SAED characterization for Cu₂Se-NC. As shown in the thermogravimetric analysis (TGA, Figure 2b), the weight change could be divided to several steps: (i) the temperature between 30 to 120 °C is likely due to the evaporation of water remaining; (ii) the 49.4% weight loss from 340 to 410 °C is attributed to the carbon combustion; (iii) the range of 410–550 °C could be estimated from the oxidation of Cu₂Se into CuO, whereby the content of 29% is Cu₂Se for Cu₂Se-NC composite [22]. The elemental composition and valence state of Cu₂Se-NC were investigated by XPS analysis (Figure S2a). In the high-resolution Cu 2p spectrum (Figure 2c), the peaks at 952.4 and 932.6 eV are attributed to Cu⁺ in Cu₂Se, and the peak at 954.4 and 934.6 eV could be assigned to the presence of Cu²⁺ in surface oxidized CuO [15,23]. For the XPS spectrum of Se 3d (Figure 2d), two major peaks located at 55.5 eV (Se 3d_{3/2}) and 54.2 eV (Se 3d_{5/2}) are ascribed to Cu-Se bonds [24]. The O 1s spectra (Figure S2b) shows the peaks with binding energies of 532.4, 531.4 and 530.6 eV can be associated with absorbed water, C–O bond and Cu–O bond for Cu₂Se-NC, respectively [25]. The N 1s spectrum (Figure S2c) is deconvoluted into representative peaks centered at 401.5, 400.0, 398.9 and 398.3 eV, attributing to oxidized-N, graphitic-N, pyrrole-N and pyridine-N, further confirming the successful nitrogen doping into Cu₂Se-NC composite [26]. The C 1 s region

(Figure S2d) is assembled in four components for the C–O (289.2 eV), C–N (286.3 eV), sp^3 C–C (285.2 eV) and sp^2 C=C bonds (284.6 eV) [27]. The existence of a carbon framework can improve the electronic conductivity and inhibit effectively volume expansion, which is favorable for fast electron transfer and structural stability during repeated cycling.

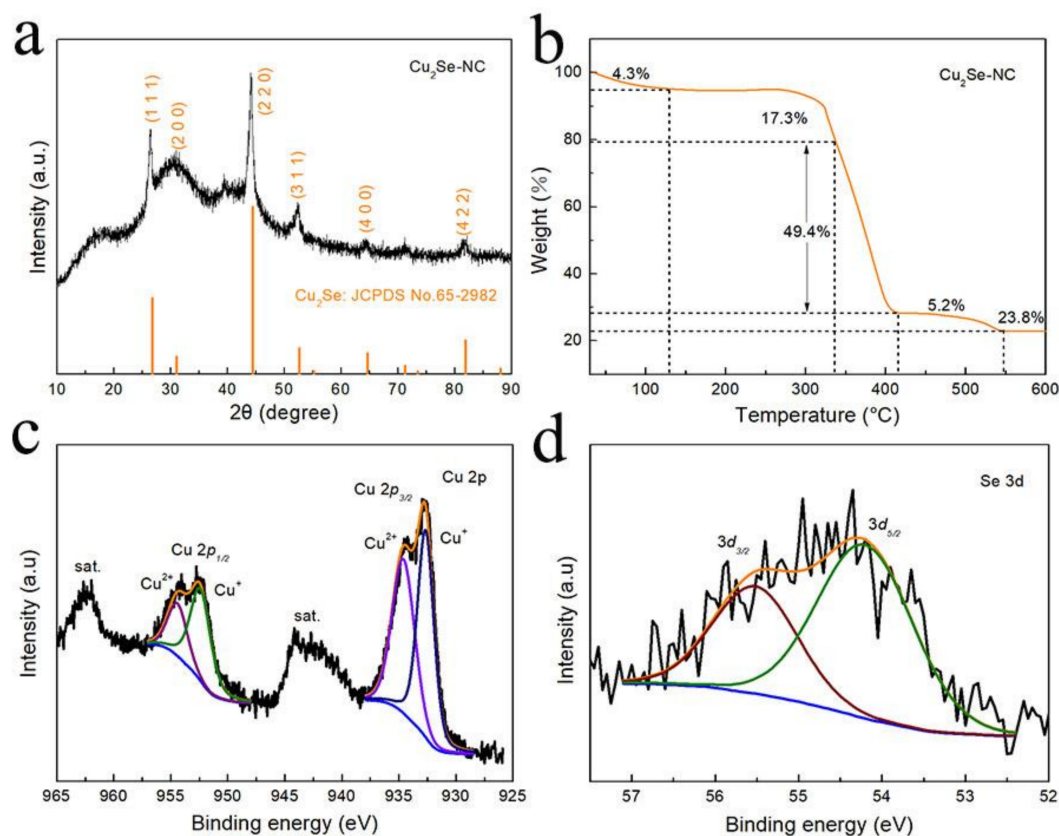


Figure 2. (a) XRD pattern of Cu_2Se -NC; (b) TGA spectra of Cu_2Se -NC; XPS spectra of (c) Cu 2p; (d) Se 3d of the Cu_2Se -NC, respectively.

Figure 3a displays the CV curves of the Cu_2Se -NC. At around 0.21 and 0.85 V of reduction process in the initial CV curve, there are obviously irreversible peaks, corresponding to the irreversible reduction of electrolyte and the formation of solid electrolyte interphase (SEI) film [28]. In the subsequent cycles, the broad reduction peak at ~ 0.7 V might be assigned to the formation of Na_2Se , and the two oxidation peaks at 0.45 and 1.55 V are assigned to the extraction of Na^+ from Na_2Se . The CV curves are well overlapped from the second cycle, demonstrating excellent electrochemical reversibility of the Cu_2Se -NC electrode. Figure 3b shows the charge–discharge profiles of the initial four cycles of Cu_2Se -NC electrode at a current density of $0.1 A g^{-1}$. The Cu_2Se -NC electrode yields a first discharge/charge specific capacity of $412/192 mA h g^{-1}$, which was higher than those of Cu_2Se (Figure S3, $322/189 mA h g^{-1}$) and NC (Figure S4, $269/73 mA h g^{-1}$). The initial Coulombic efficiency of Cu_2Se -NC electrode is 46.6%, which is consistent with the CV test results [29]. The cycling performance of the Cu_2Se -NC, Cu_2Se and NC anode for SIBs at a current density of $0.1 A g^{-1}$ is shown in Figure 3c. Cu_2Se -NC maintains a reversible capacity of $172 mA h g^{-1}$ after 200 cycles. However, the capacity of Cu_2Se is sharply decreased to $10 mA h g^{-1}$ from $189 mA h g^{-1}$ after 10 cycles, suggesting 1D carbon fiber network provides more stable structure networks for accommodation of volume expansion to ensure cycling stability. The specific capacity of NC is only $70 mA h g^{-1}$ due to the sluggish reaction kinetics of NC for SIBs.

The rate performance of the Cu_2Se -NC, Cu_2Se and NC anode is illustrated in Figure 3d. The Cu_2Se -NC electrode exhibits a high specific capacity of 193, 176, 148, 126, and $99 mA h g^{-1}$ at the current densities of 0.1, 0.2, 0.5, 1, and $2 A g^{-1}$. The specific capacity of $188 mA h g^{-1}$ can be

obtained, when current density is returned to 0.1 A g^{-1} , revealing the outstanding reversibility of the $\text{Cu}_2\text{Se-NC}$. While the capacity of Cu_2Se and NC decreases to only 3 and 24 mAh g^{-1} at 2 A g^{-1} , indicating a significant enhancement of the electrochemical performance resulting from nanosized- Cu_2Se embedded 1D nitrogen doped carbon nanofibers. Moreover, as depicted in Figure 3e, the $\text{Cu}_2\text{Se-NC}$ also exhibits favorable long-term cycling performance. After activation for five cycles, the $\text{Cu}_2\text{Se-NC}$ anode shows capacity retention of 99% (101 mAh g^{-1}) after 2000 cycles, further implying the strong stability of the 1D nanofiber structure.

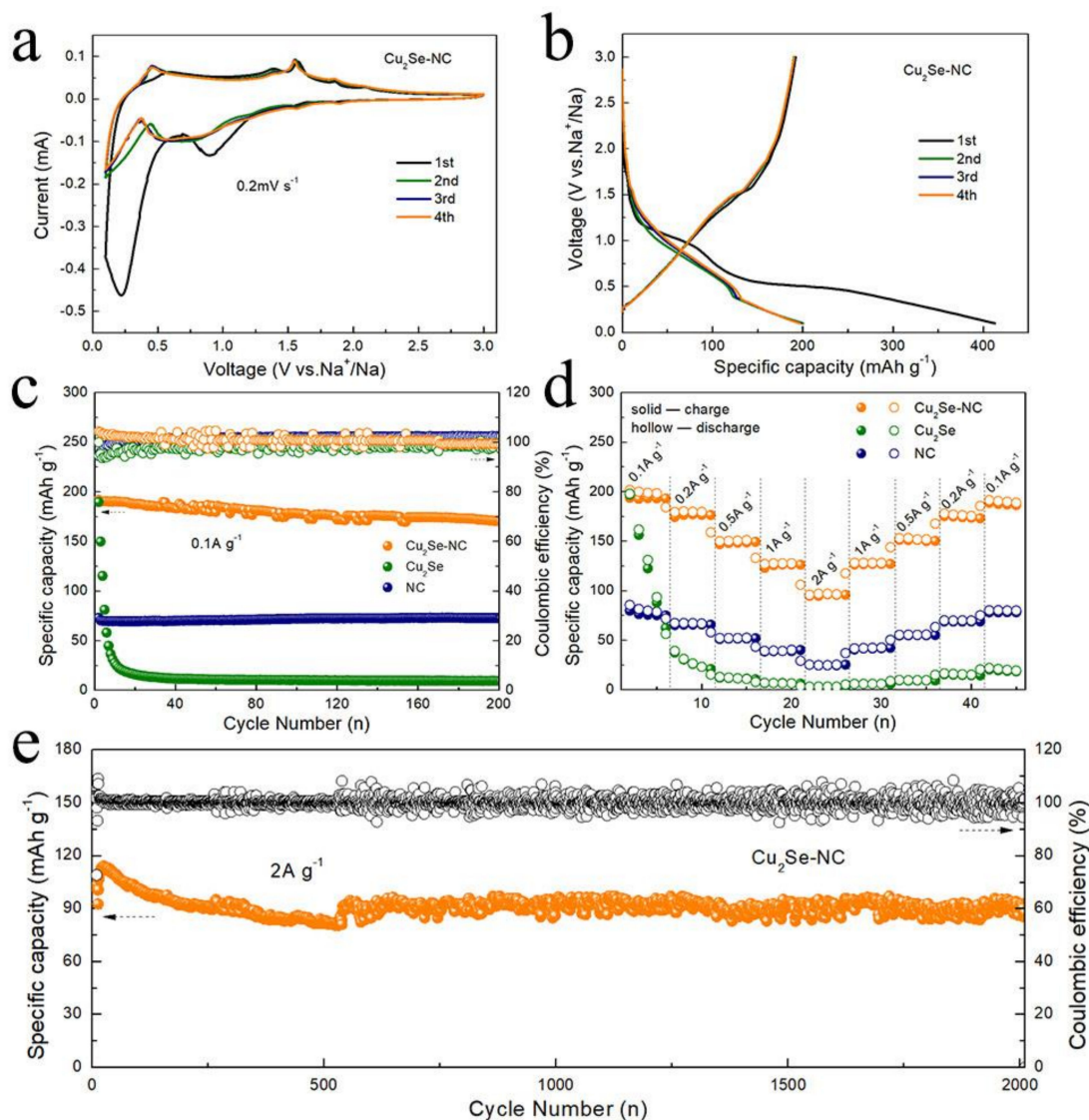


Figure 3. (a) Cyclic voltammograms of the $\text{Cu}_2\text{Se-NC}$ for the initial four cycles; (b) Charge/discharge curves of the $\text{Cu}_2\text{Se-NC}$; (c) Cycling performance and of the $\text{Cu}_2\text{Se-NC}$ and Cu_2Se and NC at 0.1 A g^{-1} ; (d) Rate capability of the $\text{Cu}_2\text{Se-NC}$ at various current densities; (e) Long cycling performance of the $\text{Cu}_2\text{Se-NC}$ at 2 A g^{-1} .

The kinetic analysis was investigated to further explain the excellent rate capability of $\text{Cu}_2\text{Se-NC}$. Figure 4a depicts the CV curves at various sweep rates (from 0.2 to 1.0 mV s^{-1}). The relationship between the peak current (*i.e.*, mA) and sweep rate (v , mV s^{-1}) and obeys the equation of $i = av^b$ that b value of 0.5 or 1.0 implies diffusion-controlled or capacitive-controlled processes, respectively [30,31]. The b value is identified by the slopes of $\log(i)$ vs. $\log(v)$ in Figure 4b. The $\text{Cu}_2\text{Se-NC}$ possesses high b values for both cathodic (0.86, 0.84) and anodic (0.74, 0.78) peaks, indicating the surface capacitive-controlled processes. This is responsible for the fast reaction kinetics and ensures considerable rate performance.

To qualify the predominated storage capacity contribution, the capacity can be divided into capacitive (k_1) and diffusion (k_2) according to $i = k_1v^{1/2} + k_2v$ ($i/v^{1/2} = k_1 + k_2v^{1/2}$) [32,33]. As shown in Figure 4c, the capacitive contributions of Cu₂Se-NC at 0.6 mV s⁻¹ are calculated as 64.9%, which indicates that Cu₂Se-NC possesses fast Na⁺ intercalation/deintercalation. Furthermore, Figure 4d displays the surface pseudocapacitive contribution in the Cu₂Se-NC increases to 72.6% as the sweep rate elevates to 1.0 mV s⁻¹. The high ratio of surface capacitive contribution is beneficial to the rate performance, which agrees with the favorable rate capability of Cu₂Se-NC (Figure 3d).

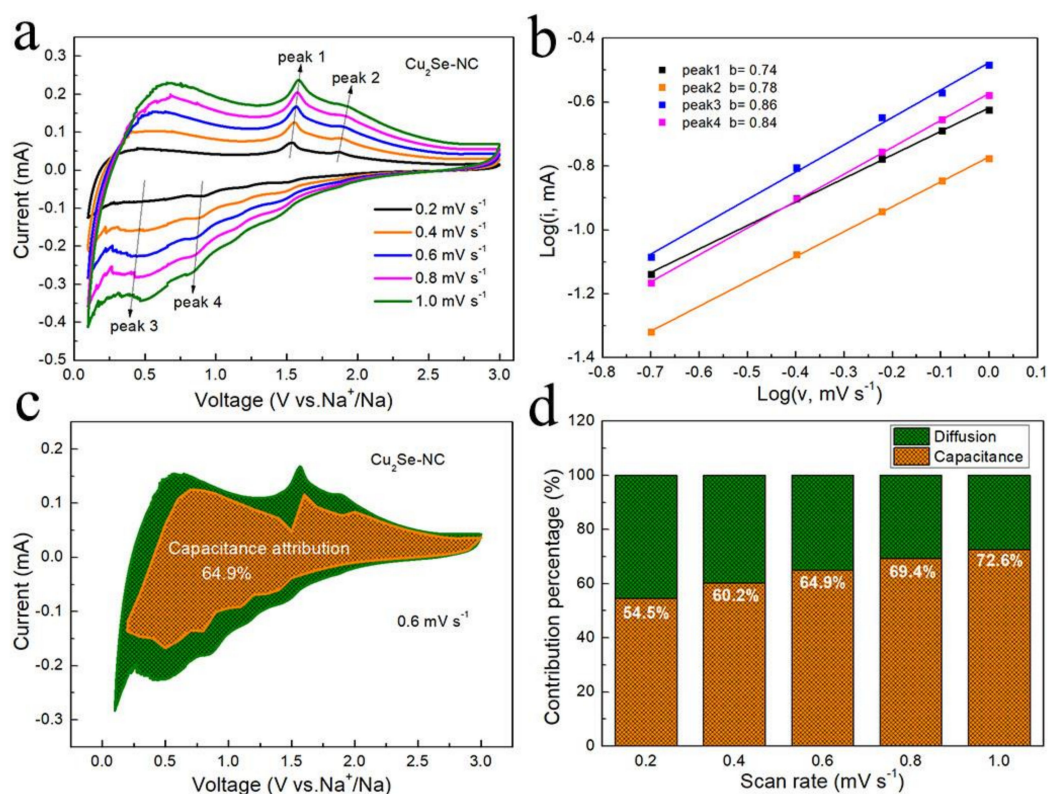


Figure 4. (a) CV curves at various scan rates of the Cu₂Se-NC (0.2, 0.4, 0.6, 0.8 and 1.0 mV s⁻¹); (b) log(*i*)-log(*v*) plots of the Cu₂Se-NC; (c) capacitive contribution and diffusion contribution at 0.6 mV s⁻¹; (d) capacitive and diffusion contribution versus scan rate of Cu₂Se-NC.

The EIS curves and equivalent electrical circuit of Cu₂Se-NC and Cu₂Se are shown in Figure 5 and inset. Before cycling, the charge-transfer resistance (R_{ct}) of Cu₂Se-NC and Cu₂Se is 1225 and 242 Ω , which decreases to 130 Ω and increases 466 Ω after 100 cycles, respectively. The decrease in resistance of Cu₂Se-NC electrode is due to the activation process during repeated cycling, resulting in faster electron transfer for SIBs. In contrast, the R_{ct} of the Cu₂Se increased significantly R_{ct} after cycles, which might be ascribed to cracking and pulverization of Cu₂Se caused by volume expansion. The diffusivity coefficient of sodium ions (D_{Na^+}) is obtained by EIS measurements based on $D = R^2T^2/(2n^4A^2F^4C^2b^2)$ and $Z' = R_e + R_{ct} + b\omega^{-1/2}$ equations [34]. Here, ω is the low range angular frequency of EIS, and b is the Warburg factor that is the slope of the line $Z' \sim \omega^{-1/2}$. Obviously, the slope b of Cu₂Se-NC is much lower than that of Cu₂Se after cycled, and the sodium-ion diffusion coefficient of Cu₂Se-NC and Cu₂Se are calculated as $\sim 3.4 \times 10^{-21}$ and 5.4×10^{-22} cm² s⁻¹, respectively. The higher D_{Na^+} of Cu₂Se-NC electrode indicates fast diffusion kinetics for sodium storage.

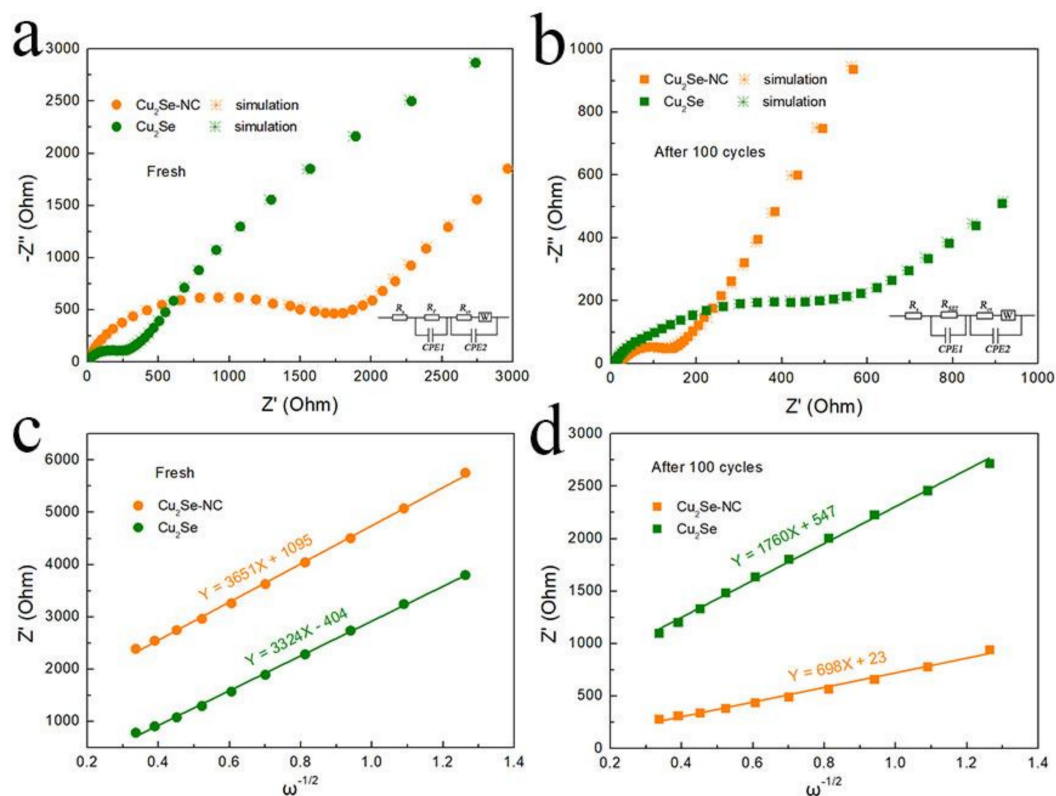


Figure 5. EIS data of $\text{Cu}_2\text{Se-NC}$ and Cu_2Se electrodes at a current density of 0.1 A g^{-1} (a) before cycling, (b) after 100 cycles; the relationship plot between Z' and $\omega^{-1/2}$ in the low-frequency region of (c) before cycling, (d) after 100 cycles.

To further prove the structural stability of the electrode, we investigate the morphologies of the $\text{Cu}_2\text{Se-NC}$ and Cu_2Se electrode before and after 100 cycles. As illustrated in Figure 6a,b, the cycled $\text{Cu}_2\text{Se-NC}$ electrode is flat with regular nanofibers, which is similar to their original morphology (Figure S5a,b). Meanwhile, the EDS mapping of the cycled $\text{Cu}_2\text{Se-NC}$ electrode in Figure S6 shows uniform distribution of Cu, Se, N, and C in the nanofiber, demonstrating superior structural integrity during long-term cycling. In contrast, Figure 6c and d shows that the structure of cycled Cu_2Se has collapsed into dense and massive bulk, which is in accordance with the rapid capacity decay. These results represent that 1D carbon fiber networks can maintain the superior structural integrity and strong tolerance of volume changes. Ex situ XRD analysis is performed to identify the Na-storage mechanism (Figure S7). The Cu_2Se (220) peak could be detected in the pristine $\text{Cu}_2\text{Se-NC}$ electrode. When it is discharged to 0.1 V, two new peaks at 43.3° and 44.1° ascribe to (111) plane of Cu (JCPDS No. 04-0836) and (042) plane of Na_2Se (JCPDS No. 47-1699), which indicates the insertion of Na^+ into Cu_2Se and the formation of Cu and Na_2Se . After recharging to 3 V, the XRD pattern displays similar signals for Cu peak, which might be attributed to the irreversible reactions. Moreover, the Cu_2Se (220) peak could not restore to the pristine state that could be due to crystalline Cu_2Se to amorphous state, providing more active sites and fast reaction kinetics.

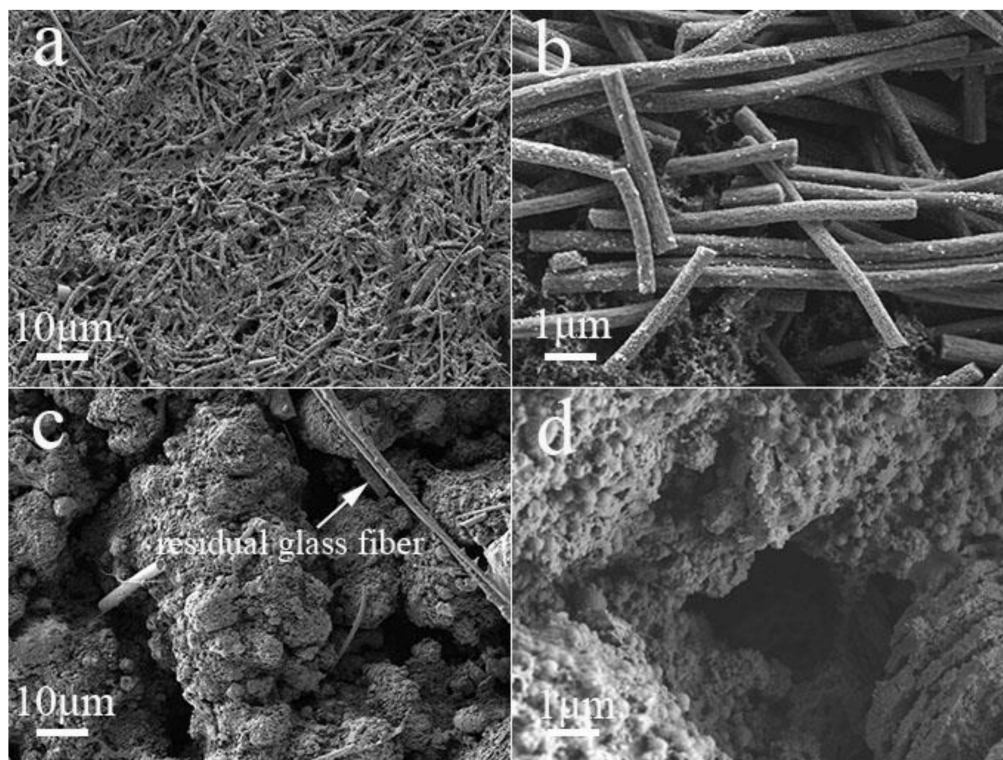


Figure 6. SEM images of (a,b) $\text{Cu}_2\text{Se-NC}$ and (c,d) Cu_2Se electrode after 100 cycles.

4. Conclusions

In summary, $\text{Cu}_2\text{Se-NC}$ was successfully fabricated and evaluated as anode materials for sodium storage. Corresponding CV kinetic analysis and D_{Na^+} calculation indicates the $\text{Cu}_2\text{Se-NC}$ possesses dominant surface pseudocapacity contribution and fast Na^+ migration, which ensures favorable rate performance for SIBs. Moreover, the carbon fibers networks afford a conductive and protective layer for the effective accommodation of volume changes to ensure their superior long cycle life. Thus, the as-prepared $\text{Cu}_2\text{Se-NC}$ electrode displays enhanced sodium storage properties with the high reversible capacity of 172 mAh g^{-1} (0.1 A g^{-1}), considerable rate capability of 99 mAh g^{-1} (2 A g^{-1}) and ultra-long cycling stability (99% capacity retention over 2000 cycles).

Supplementary Materials: The following are available online at <http://www.mdpi.com/2079-4991/10/2/302/s1>, Figure S1: Typical SEM image of Cu_2Se ; Figure S2: (a) High-resolution XPS survey spectra and corresponding (b) O 1s and (c) N 1s and (d) C 1s of the $\text{Cu}_2\text{Se-NC}$, respectively; Figure S3. Charge/discharge curves of the Cu_2Se ; Figure S4. The SEM images and Charge/discharge curves of the NC; Figure S5. SEM images of (a, b) $\text{Cu}_2\text{Se-NC}$ and (c, d) Cu_2Se electrode before cycle at a current density of 0.1 A g^{-1} ; Figure S6. SEM image and corresponding elemental mappings of the cycled $\text{Cu}_2\text{Se-NC}$. Figure S7. Ex situ XRD patterns of the $\text{Cu}_2\text{Se-NC}$ anode under different state: pristine, discharge to 0.1 V, and charge to 3 V, respectively.

Author Contributions: Writing—original draft, L.H.; Writing—review & editing, C.S.; Funding acquisition, X.W.; Resources, E.M.A., X.W. and G.Z. All authors have read and agreed to the published version of the manuscript.

Funding: This research was funded by the National Natural Science Foundation of China Program (No. 51602111); the Natural Science Foundation of Guangdong Province (2018A030313739); Cultivation project of National Engineering Technology Center (2017B090903008); Xijiang R&D Team (X.W.), Guangdong Provincial Grant (2017A050506009); Special Fund Project of Science and Technology Application in Guangdong (2017B020240002) and 111 projects; Guangdong Innovative and Entrepreneurial Team Program (No. 2016ZT06C517).

Conflicts of Interest: The authors declare no conflicts of interest.

References

1. Fu, L.; Zhang, C.; Chen, B.; Zhang, Z.; Wang, X.; Zhao, J.; He, J.; Du, H.; Cui, G. Graphene boosted Cu_2GeS_3 for advanced lithium-ion batteries. *Inorg. Chem. Front.* **2017**, *4*, 541–546. [[CrossRef](#)]
2. Shang, C.; Dong, S.; Zhang, S.; Hu, P.; Zhang, C.; Cui, G. A Ni_3S_2 -PEDOT monolithic electrode for sodium batteries. *Electrochem. Commun.* **2015**, *50*, 24–27. [[CrossRef](#)]
3. Fu, L.; Bi, Z.; Wei, B.; Huang, L.; Zhang, X.; Chen, Z.; Liao, H.; Li, M.; Shang, C.; Wang, X. Flower-like Cu_2SnS_3 Nanostructure Materials with High Crystallinity for Sodium Storage. *Nanomaterials* **2018**, *8*, 475. [[CrossRef](#)] [[PubMed](#)]
4. Hu, Z.; Tai, Z.; Liu, Q.; Wang, S.-W.; Jin, H.; Wang, S.; Lai, W.; Chen, M.; Li, L.; Chen, L.; et al. Ultrathin 2D TiS_2 Nanosheets for High Capacity and Long-Life Sodium Ion Batteries. *Adv. Energy Mater.* **2019**, *9*, 1803210. [[CrossRef](#)]
5. Liu, Z.; Lu, T.; Song, T.; Yu, X.-Y.; Lou, X.W.; Paik, U. Structure-designed synthesis of FeS_2 @C yolk-shell nanoboxes as a high-performance anode for sodium-ion batteries. *Energy Environ. Sci.* **2017**, *10*, 1576–1580. [[CrossRef](#)]
6. Li, X.; Sun, M.; Ni, J.; Li, L. Template-Free Construction of Self-Supported Sb Prisms with Stable Sodium Storage. *Adv. Energy Mater.* **2019**, *9*, 1901096. [[CrossRef](#)]
7. Zhao, Q.; Bi, R.; Cui, J.; Yang, X.; Zhang, L. TiO_{2-x} Nanocages Anchored in N-Doped Carbon Fiber Films as a Flexible Anode for High-Energy Sodium-Ion Batteries. *ACS Appl. Energy Mater.* **2018**, *1*, 4459–4466. [[CrossRef](#)]
8. Li, B.; Liu, Y.; Jin, X.; Jiao, S.; Wang, G.; Peng, B.; Zeng, S.; Shi, L.; Li, J.; Zhang, G. Designed Formation of Hybrid Nanobox Composed of Carbon Sheathed CoSe_2 Anchored on Nitrogen-Doped Carbon Skeleton as Ultrastable Anode for Sodium-Ion Batteries. *Small* **2019**, *15*, 1902881. [[CrossRef](#)]
9. Yang, C.; Feng, J.; Lv, F.; Zhou, J.; Lin, C.; Wang, K.; Zhang, Y.; Yang, Y.; Wang, W.; Li, J.; et al. Metallic Graphene-Like VSe_2 Ultrathin Nanosheets: Superior Potassium-Ion Storage and Their Working Mechanism. *Adv. Mater.* **2018**, *30*, 1800036. [[CrossRef](#)]
10. Fang, Y.; Yu, X.Y.; Lou, X.W.D. Formation of Hierarchical Cu-Doped CoSe_2 Microboxes via Sequential Ion Exchange for High-Performance Sodium-Ion Batteries. *Adv. Mater.* **2018**, *30*, 1706668. [[CrossRef](#)]
11. Yousaf, M.; Wang, Y.; Chen, Y.; Wang, Z.; Firdous, A.; Ali, Z.; Mahmood, N.; Zou, R.; Guo, S.; Han, R.P.S. A 3D Trilayered CNT/ MoSe_2 /C Heterostructure with an Expanded MoSe_2 Interlayer Spacing for an Efficient Sodium Storage. *Adv. Energy Mater.* **2019**, *9*, 1900567. [[CrossRef](#)]
12. Fu, L.; Wang, X.; Ma, J.; Zhang, C.; He, J.; Xu, H.; Chai, J.; Li, S.; Chai, F.; Cui, G. Graphene-Encapsulated Copper tin Sulfide Submicron Spheres as High-Capacity Binder-Free Anode for Lithium-Ion Batteries. *ChemElectroChem* **2017**, *4*, 1124–1129. [[CrossRef](#)]
13. Shang, C.; Hu, L.; Fu, L.; Huang, L.; Xue, B.; Wang, X.; Shui, L.; Zhou, G. Improving lithium storage capability of ternary Sn-based sulfides by enhancing inactive/active element ratio. *Solid State Ion.* **2019**, *337*, 47–55. [[CrossRef](#)]
14. Lin, J.; Lim, J.M.; Youn, D.H.; Kawashima, K.; Kim, J.H.; Liu, Y.; Guo, H.; Henkelman, G.; Heller, A.; Mullins, C.B. Self-Assembled Cu-Sn-S Nanotubes with High (De)Lithiation Performance. *ACS Nano* **2017**, *11*, 10347–10356. [[CrossRef](#)] [[PubMed](#)]
15. Yue, J.L.; Sun, Q.; Fu, Z.W. Cu_2Se with facile synthesis as a cathode material for rechargeable sodium batteries. *Chem. Commun.* **2013**, *49*, 5868–5870. [[CrossRef](#)] [[PubMed](#)]
16. Wang, X.; Chen, Y.; Fang, Y.; Zhang, J.; Gao, S.; Lou, X.W.D. Synthesis of Cobalt Sulfide Multi-shelled Nanoboxes with Precisely Controlled Two to Five Shells for Sodium-Ion Batteries. *Angew. Chem. Int. Ed.* **2019**, *58*, 2675–2679. [[CrossRef](#)]
17. Yang, H.; Xu, R.; Yao, Y.; Ye, S.; Zhou, X.; Yu, Y. Multicore-Shell Bi@N-doped Carbon Nanospheres for High Power Density and Long Cycle Life Sodium-and Potassium-Ion Anodes. *Adv. Funct. Mater.* **2019**, *29*, 1809195. [[CrossRef](#)]
18. Pan, Q.; Zhang, Q.; Zheng, F.; Liu, Y.; Li, Y.; Ou, X.; Xiong, X.; Yang, C.; Liu, M. Construction of MoS_2 /C Hierarchical Tubular Heterostructures for High-Performance Sodium Ion Batteries. *ACS Nano* **2018**, *12*, 12578–12586. [[CrossRef](#)]

19. Yin, H.; Li, Q.; Cao, M.; Zhang, W.; Zhao, H.; Li, C.; Huo, K.; Zhu, M. Nanosized-bismuth-embedded 1D carbon nanofibers as high-performance anodes for lithium-ion and sodium-ion batteries. *Nano Res.* **2017**, *10*, 2156–2167. [[CrossRef](#)]
20. Li, Z.; Fang, Y.; Zhang, J.; Lou, X.W.D. Necklace-Like Structures Composed of Fe₃N@C Yolk-Shell Particles as an Advanced Anode for Sodium-Ion Batteries. *Adv. Mater.* **2018**, *30*, 1800525. [[CrossRef](#)]
21. Ma, D.; Li, Y.; Mi, H.; Luo, S.; Zhang, P.; Lin, Z.; Li, J.; Zhang, H. Robust SnO_{2-x} Nanoparticle-Impregnated Carbon with Outstanding Electrochemical Performance for Advanced Sodium-Ion Batteries. *Angew. Chem. Int. Ed.* **2018**, *57*, 8901–8905. [[CrossRef](#)] [[PubMed](#)]
22. Cho, J.S.; Lee, S.Y.; Kang, Y.C. First Introduction of NiSe₂ to Anode Material for Sodium-Ion Batteries: A Hybrid of Graphene-Wrapped NiSe₂/C Porous Nanofiber. *Sci. Rep.* **2016**, *6*, 23338. [[CrossRef](#)] [[PubMed](#)]
23. Lin, H.; Li, M.; Yang, X.; Yu, D.; Zeng, Y.; Wang, C.; Chen, G.; Du, F. Nanosheets-Assembled CuSe Crystal Pillar as a Stable and High-Power Anode for Sodium-Ion and Potassium-Ion Batteries. *Adv. Energy Mater.* **2019**, *9*, 1900323. [[CrossRef](#)]
24. Liu, T.; Li, Y.; Zhao, L.; Zheng, F.; Guo, Y.; Li, Y.; Pan, Q.; Liu, Y.; Hu, J.; Yang, C. In Situ Fabrication of Carbon-Encapsulated Fe₇X₈ (X = S, Se) for Enhanced Sodium Storage. *ACS Appl. Mater. Interfaces* **2019**, *11*, 19040–19047. [[CrossRef](#)]
25. Yuan, C.; Li, J.; Hou, L.; Zhang, X.; Shen, L.; Lou, X.W.D. Ultrathin Mesoporous NiCo₂O₄ Nanosheets Supported on Ni Foam as Advanced Electrodes for Supercapacitors. *Adv. Funct. Mater.* **2012**, *22*, 4592–4597. [[CrossRef](#)]
26. Zhang, Y.; Su, Q.; Xu, W.; Cao, G.; Wang, Y.; Pan, A.; Liang, S. A Confined Replacement Synthesis of Bismuth Nanodots in MOF Derived Carbon Arrays as Binder-Free Anodes for Sodium-Ion Batteries. *Adv. Sci.* **2019**, *6*, 1900162. [[CrossRef](#)]
27. Shang, C.; Hu, L.; Lin, Q.; Fu, X.; Wang, X.; Zhou, G. Integration of NaV₆O₁₅·nH₂O nanowires and rGO as cathode materials for efficient sodium storage. *Appl. Surf. Sci.* **2019**, *494*, 458–464. [[CrossRef](#)]
28. Chen, W.; Zhang, X.; Mi, L.; Liu, C.; Zhang, J.; Cui, S.; Feng, X.; Cao, Y.; Shen, C. High-Performance Flexible Freestanding Anode with Hierarchical 3D Carbon-Networks/Fe₇S₈/Graphene for Applicable Sodium-Ion Batteries. *Adv. Mater.* **2019**, *31*, 1806664. [[CrossRef](#)]
29. Ou, X.; Cao, L.; Liang, X.; Zheng, F.; Zheng, H.S.; Yang, X.; Wang, J.H.; Yang, C.; Liu, M. Fabrication of SnS₂/Mn₂SnS₄/Carbon Heterostructures for Sodium-Ion Batteries with High Initial Coulombic Efficiency and Cycling Stability. *ACS Nano* **2019**, *13*, 3666–3676. [[CrossRef](#)]
30. Wang, Y.; Wang, Y.; Wang, Y.X.; Feng, X.; Chen, W.; Qian, J.; Ai, X.; Yang, H.; Cao, Y. In Situ Formation of Co₉S₈ Nanoclusters in Sulfur-Doped Carbon Foam as a Sustainable and High-Rate Sodium-Ion Anode. *ACS Appl. Mater. Interfaces* **2019**, *11*, 19218–19226. [[CrossRef](#)]
31. Ni, Q.; Bai, Y.; Guo, S.; Ren, H.; Chen, G.; Wang, Z.; Wu, F.; Wu, C. Carbon Nanofiber Elastically Confined Nanoflowers: A Highly Efficient Design for Molybdenum Disulfide-Based Flexible Anodes Toward Fast Sodium Storage. *ACS Appl. Mater. Interfaces* **2019**, *11*, 5183–5192. [[CrossRef](#)] [[PubMed](#)]
32. Jiang, Y.; Song, D.; Wu, J.; Wang, Z.; Huang, S.; Xu, Y.; Chen, Z.; Zhao, B.; Zhang, J. Sandwich-like SnS₂/Graphene/SnS₂ with Expanded Interlayer Distance as High-Rate Lithium/Sodium-Ion Battery Anode Materials. *ACS Nano* **2019**, *13*, 9100–9111. [[CrossRef](#)] [[PubMed](#)]
33. Gan, Q.; He, H.; Zhu, Y.; Wang, Z.; Qin, N.; Gu, S.; Li, Z.; Luo, W.; Lu, Z. Defect-Assisted Selective Surface Phosphorus Doping to Enhance Rate Capability of Titanium Dioxide for Sodium Ion Batteries. *ACS Nano* **2019**, *13*, 9247–9258. [[CrossRef](#)] [[PubMed](#)]
34. Chen, W.; Qi, S.; Yu, M.; Feng, X.; Cui, S.; Zhang, J.; Mi, L. Design of FeS₂@rGO composite with enhanced rate and cyclic performances for sodium ion batteries. *Electrochim. Acta* **2017**, *230*, 1–9. [[CrossRef](#)]

